Synthesis and electrochemical characterizations of poly(3,4-ethylenedioxythiophene/manganese oxide coated on porous carbon nanofibers as a

Energy Reports 7 (2021) 8677–8687

Contents lists available at ScienceDirect

Energy Reports

journal homepage: www.elsevier.com/locate/egyr

Research paper

Synthesis and electrochemical characterizations of poly(3,4-ethylenedioxythiophene/manganese oxide coated on porous carbon nanofibers as a potential anode for lithium-ion batteries

Muhammad Amirul Aizat Mohd Abdah [a], Marliyana Mokhtar [a], Lee Tian Khoon [b,c,*], Kamaruzzaman Sopian [a], Nurul Akmaliah Dzulkurnain [b], Azizan Ahmad [b,c], Yusran Sulaiman [d,e], Federico Bella [f,g,**], Mohd Sukor Su'ait [a]

[a] Solar Energy Research Institute, Universiti Kebangsaan Malaysia, 43600 Bangi, Selangor, Malaysia
[b] School of Chemical Sciences, Faculty of Science and Technology, Universiti Kebangsaan Malaysia, 43600 Bangi, Selangor, Malaysia
[c] Research Center for Quantum Engineering Design, Faculty of Science and Technology, Universitas Airlangga, 60115 Surabaya, Indonesia
[d] Department of Chemistry, Faculty of Science, Universiti Putra Malaysia, 43400 Serdang, Selangor, Malaysia
[e] Functional Devices Laboratory, Institute of Advanced Technology, Universiti Putra Malaysia, 43400 Serdang, Selangor, Malaysia
[f] Department of Applied Science and Technology, Politecnico di Torino, Corso Duca degli Abruzzi 24, 10129 Torino, Italy
[g] National Interuniversity Consortium of Material Science and Technology (INSTM), Via Giuseppe Giusti 9, 50121 Firenze, Italy

ARTICLE INFO

Article history:
Received 30 August 2021
Received in revised form 9 October 2021
Accepted 27 October 2021
Available online xxxx

Keywords:
Carbon nanofibers
Conducting polymer
Manganese oxide
Synergistic effect
Lithium-ion batteries

ABSTRACT

Poly(3,4-ethylenedioxythiophene)/manganese oxide coated on porous carbon nanofibers (P-CNFs/PEDOT/MnO_2) is developed as an advanced anode material via the innovative combination of multiple routes, such as electrospinning, carbonization and electrodeposition. The structural and morphological characterization of the P-CNFs/PEDOT/MnO_2 electrode indicates that crosslinked and rough surface provides, as a strategic point, enough active sites for Li^+ storage. PEDOT nanoparticles and irregular block shape of MnO_2 are randomly oriented on the P-CNFs surface, thus allowing a possible electron-conducting pathway, increment in catalytic activity as well as a buffer of the volumetric changes upon cycling. Consequently, the obtained P-CNFs/PEDOT/MnO_2 electrode exhibits a truly promising electrochemical performance, which displays discharge capacity of 1477 mAh/g, better than that of P-CNFs/PEDOT (1191 mAh/g), P-CNFs/MnO_2 (763 mAh/g) and P-CNFs (433 mAh/g), at a current density of 2 mA/g. In addition, satisfactory electrochemical performances of the as-prepared P-CNFs/PEDOT/MnO_2 electrode after 20 cycles of charge/discharge are detected, with a Coulombic efficiency higher than 90% and a charge-transfer resistance being relatively smaller (131.91 Ω) than that of P-CNFs/PEDOT (232.66 Ω) and P-CNFs/MnO_2(169.17 Ω) electrodes. Thus, these results indicate that the P-CNFs/PEDOT/MnO_2 electrode could offer a great potential to replace commercial graphite for lithium-ion batteries.

1. Introduction

In the past several decades, the increasing demand for energy growth has gained widespread attention because of the fast depletion of fossil fuels and huge demand for an alternative and clean energy sources (Carley and Konisky, 2020; Baumann et al., 2020). To overcome this existing environmental crisis, much efforts have been devoted in developing sustainable and renewable energy storage systems (Xu et al., 2021; Li et al., 2021). Among the non-conventional energy storage devices, lithium-ion batteries (LIBs) are playing very important roles in a broad range of practical applications (Chen et al., 2021; Fantham and Gladwin, 2021; Rowden and Garcia-Araez, 2021), particularly in portable electronics and electric vehicles (EVs), owing to their high energy density, high capacities and long cycling life (Jin et al., 2019; Ouyang et al., 2020; Lee et al., 2019; Hannan et al., 2017; Khoon et al., 2019). In general, LIBs are composed of anode (negative electrode), cathode (positive electrode), a separator between the two electrodes and an electrolyte (Shadike et al., 2021; Hao et al., 2021; Wang et al., 2020). During charging process, lithium ions (Li^+) are transferred from the cathode to the anode through the electrolyte and the current flows from anode to cathode. When

* Corresponding author at: School of Chemical Sciences, Faculty of Science and Technology, Universiti Kebangsaan Malaysia, 43600 Bangi, Selangor, Malaysia.
** Corresponding author at: Department of Applied Science and Technology, Politecnico di Torino, Corso Duca degli Abruzzi 24, 10129 Torino, Italy.
E-mail addresses: tiankhoon@ukm.edu.my (L.T. Khoon), federico.bella@polito.it (F. Bella).

https://doi.org/10.1016/j.egyr.2021.10.110

the battery is discharged, the anode undergoes oxidation, or loss of electrons, in which Li^+ ions are released from anode and migrate back to cathode. **Figure S1** displays the basic mechanism of a LIB system. As one of the important components of LIBs, electrode materials, especially anodes, have continuously been the research focus as they play a vital role in the electrochemical performance (Sun et al., 2020; Chen et al., 2016). A rationally designed anode electrode could exhibit fascinating advantages; it provides additional active sites for Li^+ storage, possesses an excellent electronic/ionic conductivity with shortened pathways for fast Li^+ diffusion and electron transport (Liang et al., 2016). To date, carbonaceous materials (including graphite (Zhu and Ding, 2019), graphene (Zhang et al., 2019b), carbon nanotubes (CNTs) (Bai et al., 2019) and carbon nanofibers (CNFs) (Wang et al., 2015) have been reported to show an excellent electrochemical performance. Among them, three-dimensional (3D) networks of CNFs have been considered as promising anode materials due to their high specific surface area (SSA), (Zhou et al., 2016; Zainoodin et al., 2014) good electrical conductivity, providing high lithiation capability and remarkable cycling stability (Song et al., 2015). Electrospinning technique can be considered as a facile method for processing viscous polymer solutions into consecutive one-dimensional (1D) nanofibers, as well offering many opportunities to tailor the fiber morphology, chemical composition and functionality. The nonwoven fibers obtained from the electrospinning was used to produce CNFs via stabilization and subsequent carbonization processes. However, the poor specific capacity of individual CNFs remains the major bottleneck that prohibits practical application. Therefore, the incorporation of transition metal oxides (TMOs, M_xO_y with M = Ru, Co, Mn, V, Fe, Zn, etc.) with CNFs is an ideal solution to overcome the above-mentioned problem. Among various TMOs, manganese oxide (MnO_2) is one of the most widely studied in view of its good prospect for potential applications, such as an abundance of Mn source, high theoretical capacity (756 mAh/g), low operating voltage (0.5 V and 1.2 V *vs.* Li^+/Li), low-cost, non-toxicity and environmentally benignity (Lin et al., 2020). Nevertheless, MnO_2 often suffers from unsatisfactory specific capacity caused by its intrinsically poor electronic conductivity (10^{-8} to 10^{-6} S/cm) (Zheng et al., 2017), which could obstruct its practical applications. Alternatively, many attempts are made by introducing highly conducting polymers (CPs) such as poly(aniline) (PANI) (Hui et al., 2017), poly(3,4-ethylenedioxythiophene) (PEDOT) (Yan et al., 2017; Zhao et al., 2014), poly(pyrrole) (PPy) (Jin et al., 2020) and poly(thiophene) (PT) (Xu et al., 2017) to reinforce the inferior electrical conductivity of MnO_2. PEDOT has been a research hot-topic as a potential LIB anode material owing to its fast and reversible charge storage mechanism, superior electrical conductivity (300–500 S/cm), good thermal and electrochemical stabilities with low environmental pollution (Jung and Lee, 2011). For example, Liu et al. successfully prepared a $LiNi_{1/3}Co_{1/3}Mn_{1/3}O_2$/PEDOT through a simple carbonate co-precipitation and subsequent annealing approach (Liu et al., 2013), which revealed an improved specific capacity from 41.8 mAh/g to 73.9 mAh/g at current density of 1.5 A/g. Huang et al. designed a nickel oxide/PEDOT (NiO/PEDOT) film via two facile methods (H. Huang et al., 2010), *i.e.* chemical bath deposition followed by electrodeposition methods. By using NiO/PEDOT as anode, it showed an initial discharge capacity of about 1000 mAh/g, which was much greater than that of the bare NiO (600 mAh/g) at 2C. The enhancement of electrochemical properties of NiO/PEDOT film was attributed to the inclusion of PEDOT layer that provided stabilized pathways for transporting electrons and Li^+ among the NiO nanoflakes. However, it is known that pure PEDOT exhibits some inevitable shortcomings, like a severe degradation of the capacity and poor rate performance due to its structural deterioration (swelling/shrinkage) during repeated charge and discharge processes.

Herein, we present an architecture of porous CNFs/PEDOT/MnO_2 (P-CNFs/PEDOT/MnO_2) through electrospinning and carbonization assisted with electrodeposition technique. Benefiting from the unique architecture and the synergistic effect between the multiple components (3D porous CNFs providing more electrochemically active sites for ion migration/electron transfer and facilitating the formation of stable solid electrolyte interphase – SEI – film, PEDOT boosting the electronic conductivity and MnO_2 exhibiting high theoretical specific capacity as well alleviating the mechanical degradation during cycling), the P-CNFs/PEDOT/MnO_2 electrode is expected to exhibit remarkably enhanced Li-storage capabilities in terms of cycling stability, specific capacity and rate capability for advanced LIBs.

2. Experimental

2.1. Materials

Poly(acrylonitrile) (PAN, M_w = 150,000), poly (tetrafluoroethylene) (PTFE), 3,4-ethylenedioxythiophene (EDOT), Li metal, Li hexafluorophosphate ($LiPF_6$), Li perchlorate ($LiClO_4$), Mn(II) sulfate monohydrate ($MnSO_4 \cdot H_2O$, ≥99.0% purity) and silver (Ag) wire (diameter 0.5 mm) were purchased from Sigma-Aldrich and used as received. *N*,*N*-dimethylformamide (DMF), acetonitrile, sulfuric acid (H_2SO_4, 95% purity) and poly(vinylidene fluoride) (PVDF) were purchased from Merck, Systerm, Fisher Scientific and Solvay, respectively. Carbon additive (Super P) and Cu foils were obtained from KGC Resources Sdn. Bhd. Deionized (DI) water was used throughout all experiments (resistivity: 18.2 MΩ cm).

2.2. Fabrication of P-CNFs/PEDOT/MnO_2 as anode

Typically, 10 wt% PAN and PTFE were dissolved in DMF solvent under vigorous stirring at room temperature for 24 h. The optimized composition of PAN to PTFE has been reported in our previous publication (Mohd Abdah et al., 2019). A homogeneous PAN/PTFE solution was used as the precursor for the subsequent electrospinning. The electrospun solution was then loaded into a 5 mL plastic syringe using an 18-gauge blunt needle and connected to a high voltage power supply. The electrospinning was performed from the tip to the collector distance of 15 cm with an applied voltage of 15 kV and a feeding rate of 1 mL/h. The as-spun PAN/PTFE nanofibers were stabilized in oxidative atmosphere at 280 °C at a heating rate of 1 °C/min, and further carbonized at 800 °C under nitrogen (N_2) at a heating rate of 5 °C/min, forming P-CNFs. A non-aqueous EDOT solution was prepared by dissolving 10 mM EDOT monomer (10% *v*/(*v*) and 0.1 $LiClO_4$ in acetonitrile. The electropolymerization of EDOT monomer was carried out on P-CNFs via chronoamperometry at a deposition potential of 1.1 V for 15 min. Finally, MnO_2 was electrodeposited potentiostatically using a similar technique on P-CNFs/PEDOT (0.8 V, 15 min) from a solution consisting of 0.05 $MnSO_4 \cdot H_2O$ (50% *v*/(*v*) in DI water. The preparation of P-CNFs/PEDOT/MnO_2 hybrid composite (including electrodeposition of PEDOT and MnO_2) were all carried out using a three-electrode system. Fig. 1 displays the schematic illustration of P-CNFs/PEDOT/MnO_2 fabrication process.

For slurry preparation, P-CNFs/PEDOT/MnO_2, Super P and PVDF in DMF were mixed keeping a weight ratio of 85:5:10. Then, the prepared slurry was coated onto a Cu foil and dried at 80 °C for 6 h in a normal oven. A circular electrode disk (diameter: 13 mm, area: 1.6 cm^2) was punched and further heated at 120 °C in vacuum oven for several hours. The mass loading of P-CNFs/PEDOT/MnO_2 electrode was 2.92 mg/cm^2.

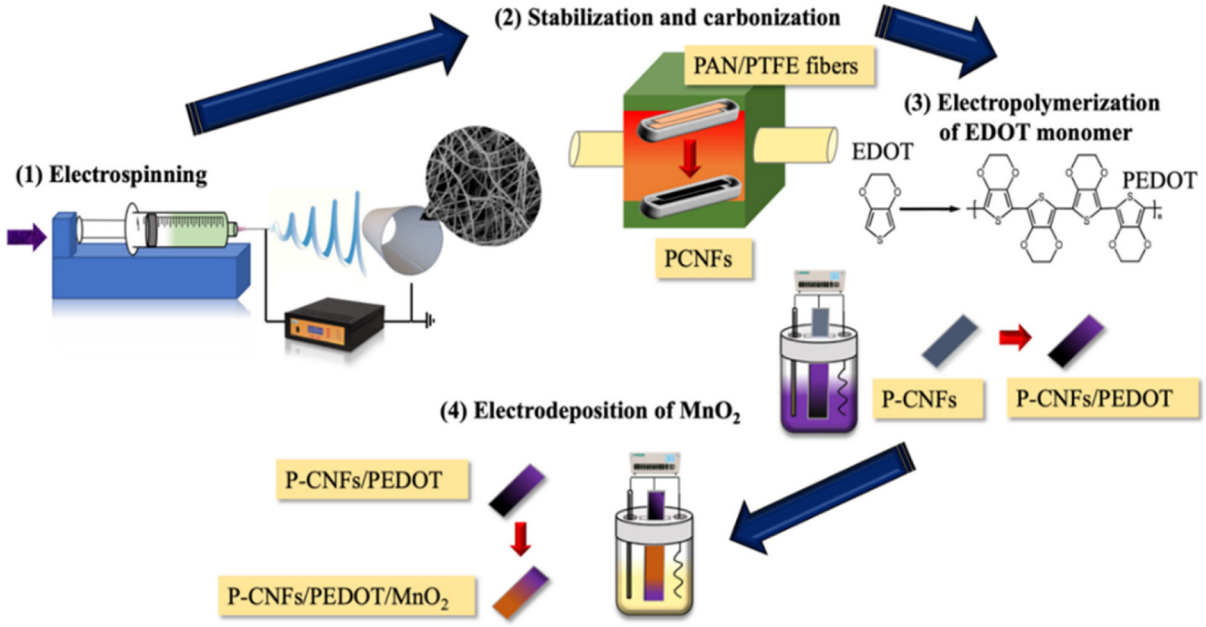

Fig. 1. Schematic illustration of the synthetic process of P-CNFs/PEDOT/MnO_2 hybrid composite.

2.3. Characterizations

The surface morphology and elemental composition of as-prepared electrodes were observed by field emission scanning electron microscope (FESEM) with energy dispersive spectroscopy (EDX) (Merlin Compact). X-ray diffraction (XRD) patterns of the electrodes were recorded by a Bruker D8-Advance using Cu Kα as the X-rays source ($\lambda = 1.54$ Å). Raman spectra were examined using a DXR 2xi Raman Imaging Microscope with a 532 nm laser. The electrode surface species and their chemical states were studied via X-ray photoelectron spectroscopy (XPS XSAMHS Kratos Analytical) analysis. Brunauer–Emmett–Teller (BET, Micromeritics Tristar II plus) was used to analyze the SSA, pore volume and the pore size distribution (PSA) at 77 K. The surface topography, mechanical and electronic properties of the samples were studied using atomic force microscopy (AFM, Park Systems NX-10) under the tapping mode at room temperature.

The electrochemical measurements were carried out on CR 2032 type coin cells. The coin cells were assembled in an argon Ar-filled glove box (moisture and – O_2 – levels lower than 1.0 ppm). Celgard 2400 membrane was used as a separator and the electrolyte was prepared by dissolving 1 mol/L of $LiPF_6$ in ethylene carbonate (EC) and dimethyl carbonate (DMC) (volume ratio 1:1) with Li metal as the counter and reference electrode. The assembled cells were put in rest for 12 h before electrochemical measurements were taken. Charge and discharge characteristics were galvanostatically tested between 0.01–2 V for *vs.* Li^+/Li at ambient temperature using a Neware Battery Testing System. Cyclic voltammetry (CV, at 0.1 mV/s) and electrochemical impedance spectroscopy (EIS, with frequency varied from 1 MHz to 0.01 Hz at a potential amplitude of 5 mV) were performed using an electrochemical workstation (Versastat4, Princeton).

Overall, main characterization techniques adopted in currently investigated energy materials are adopted when not specified differently (Liao et al., 2019; Li et al., 2019; Ogawa and Mori, 2019; Augustine et al., 2019; Liu et al., 2019b; Lehmann et al., 2019; Zhang et al., 2019a; Kumar et al., 2019; Choudhury et al., 2019; Galluzzo et al., 2019).

3. Results and discussion

3.1. Characterization of P-CNFs/PEDOT/MnO_2 electrodes

Surface morphology of as-prepared P-CNFs, P-CNFs/MnO_2, P-CNFs/PEDOT and P-CNFs/PEDOT/MnO_2 electrodes were examined through FESEM analysis, as shown in Fig. 2. All samples (Fig. 2a–d) show a 3D interconnected network of CNFs. According to Wu et al., this interconnected network of CNFs was expected to shorten the diffusion length of Li^+ and enhance the rapid transfer of electrons during charge/discharge (Ao et al., 2020). The inset of Fig. 2a shows the FESEM image of bare P-CNFs, which display a rough and groove surface resulting from the decomposition of the sacrificial polymer, *i.e.* PTFE, during carbonization (Tran and Kalra, 2013; Hu et al., 2020; Ju et al., 2017) with an average diameter of 471 ± 90 nm. After bare P-CNFs were mixed with PVDF and Super P to prepare the electrode (Fig. 2a), it can be seen that fractured CNFs surfaces were observed, whereas the nodular morphology of PVDF binder and the spherical-like nanoparticles of Super P were randomly distributed and filled the void space between the fractured P-CNFs. Interestingly, some of the carbon nanospheres are aggregated to form a 3D sponge-like architecture, which is beneficial to facilitate the migration of Li^+ between the active material and electrolyte as well relieves the volume expansion/shrinkage of PEDOT during repeated charge–discharge cycles (Gao et al., 2011). The inset of FESEM image of P-CNFs/PEDOT (Fig. 2c) shows that there are plenty of small grains with a size of ≈22 nm anchored to the surface of the nanofibers, which indicates the presence of PEDOT nanoparticles which could overcome the electrode pulverization. However, it can be seen that the irregular block shape of MnO_2 was observed in FESEM image of P-CNFs/PEDOT/MnO_2 electrode (Fig. 2d) and the distinguished void spaces could greatly improve the electrochemical Li storage of batteries. In addition, Fig. 2e displays the typical EDX spectrum of P-CNFs/PEDOT/MnO_2 electrode with obvious C, S, O, F and Mn peaks. EDX elemental mapping (Fig. 2f) further verified the coexistence of C, S, O, F and Mn elements within the P-CNFs/PEDOT/MnO_2 electrode.

The surface topography with different roughness of P-CNFs, P-CNFs/MnO_2, P-CNFs/PEDOT and P-CNFs/PEDOT/MnO_2 electrodes

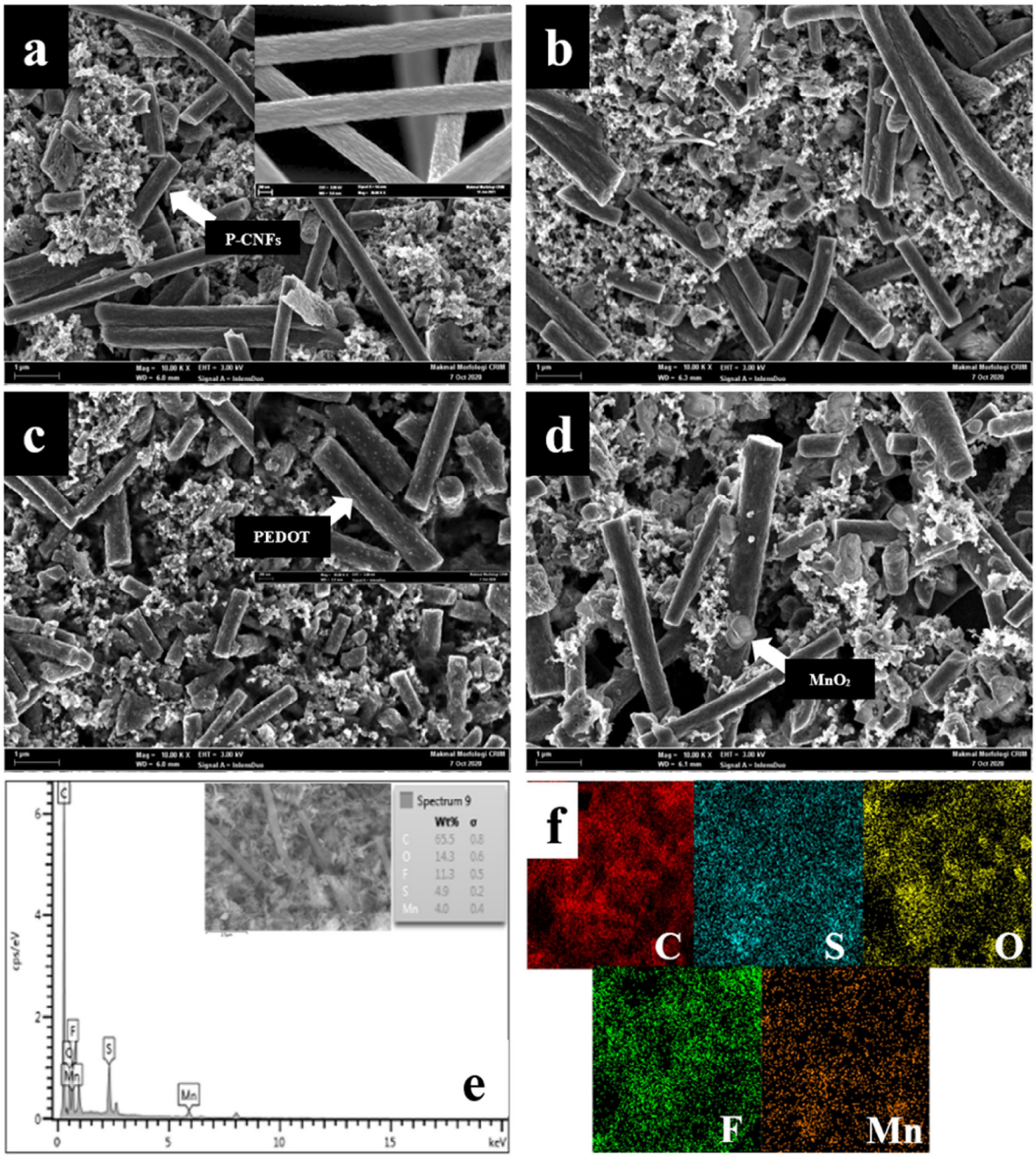

Fig. 2. FESEM images of (a) P-CNFs, (b) P-CNFs/MnO_2, (c) P-CNFs/PEDOT and (d) P-CNFs/PEDOT/MnO_2 electrodes. The insets of (a) and (b) represent the high magnification of P-CNFs composite and P-CNFs/PEDOT electrode. (e) EDX spectrum and (f) corresponding elemental mapping images of P-CNFs/PEDOT/MnO_2 electrode.

was examined via AFM analysis, as shown in Fig. 3. Table 1 indicates that P-CNFs electrode (Fig. 3a) has a smoother surface when compared with other electrodes, as revealed by the root mean square (RMS) roughness of 0.014 nm. However, it was found that the RMS surface roughness of P-CNFs/PEDOT/MnO_2 electrode (Fig. 3d) slightly increased to 0.987 nm, due to the irregular block shape of MnO_2 that randomly embedded on the surface of P-CNFs, in agreement with the FESEM image. In addition, based on XRD analysis, the formation crystal planes of tetragonal MnO_2 (JCPDS 44–0141) in P-CNFs/MnO_2 and P-CNFs/PEDOT/MnO_2 electrodes proved to increase the surface roughness. According to Xu et al., a high RMS is beneficial to induce better interface contact between electrode material and current collector, that can efficiently minimize diffusion paths for the insertion/extraction of Li^+, leading to enhanced electrochemical performance (Xu et al., 2019). The rheology-related properties of the as-prepared electrodes was further tested using contact mode cantilevers and the Hertz model was used to interpret force–distance (F–d) curve to calculate Young's modulus (E). P-CNFs/PEDOT/MnO_2 electrode exhibited a remarkable mechanical strength (E = 1.97 kPa), better than P-CNFs (1.71 kPa), P-CNFs/PEDOT (1.18 kPa) and P-CNFs/MnO_2 (0.99 kPa), validating its good load-bearing capability. Moreover, the conductance (G, S) values of the individual electrodes were measured via conductive-probe AFM (CP-AFM) and the surface conductivity (κ, S/cm) was further calculated according to the following equation (Lee et al., 2010):

$$\kappa = \frac{G \cdot L}{A}$$

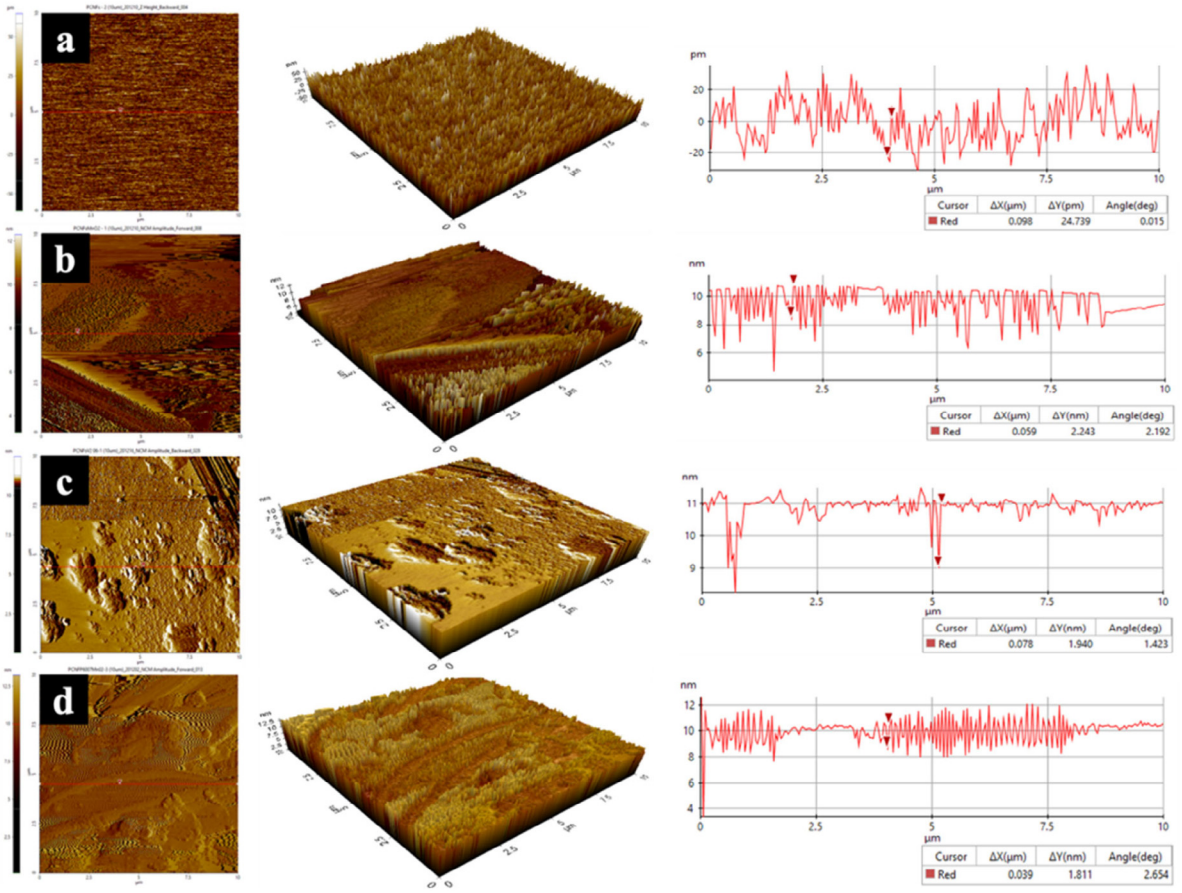

Fig. 3. AFM with topographic heights of (a) P-CNFs, (b) P-CNFs/MnO_2, (c) P-CNFs/PEDOT and (d) P-CNFs/PEDOT/MnO_2 electrodes.

Table 1
RMS roughness, E and κ values of P-CNFs, P-CNFs/MnO_2, P-CNFs/PEDOT and P-CNFs/PEDOT/MnO_2 electrodes, obtained from AFM results.

Electrode	RMS (nm)	E (kPa)	κ (S/cm)
P-CNFs	0.014	1.71	$5.14 \cdot 10^{-14}$
P-CNFs/MnO_2	1.022	0.99	$4.23 \cdot 10^{-15}$
P-CNFs/PEDOT	0.447	1.18	$2.27 \cdot 10^{-15}$
P-CNFs/PEDOT/MnO_2	0.987	1.97	$1.63 \cdot 10^{-9}$

where L and A represent the thickness (cm) and cross-sectional area (cm^2) of the electrode, respectively. It should be noted that the synergistic cooperation between hybrid materials can obviously improve the κ of P-CNFs/PEDOT/MnO_2 electrode ($1.63 \cdot 10^{-9}$ S/cm), thus contributed to high capacity and rapid electrochemical kinetics properties.

The respective BET surface areas and PSA of P-CNFs, P-CNFs/MnO_2, P-CNFs/PEDOT and P-CNFs/PEDOT/MnO_2 composites were examined via N_2 adsorption–desorption analysis, as displayed in Fig. 4a. All composites exhibited type IV isotherm, with a hysteresis loop in the p/p^0 range of 0.8–1.0, which implied the existence of a mesoporous structure (2–50 nm) (Yao et al., 2020). Based on the BET model, the SSA and the pore volume values for P-CNFs/PEDOT/MnO_2 were only 13.74 m^2/g and 0.026 cm^3/g, respectively, in comparison with P-CNFs (260.08 m^2/g and 0.199 cm^3/g), P-CNFs/MnO_2 (114.12 m^2/g and 0.096 cm^3/g) and P-CNFs/PEDOT (14.89 m^2/g and 0.033 cm^3/g). This phenomenon can be explained based on the inset in Fig. 4a, where the surface of P-CNFs was mostly covered with dense morphologies of PEDOT and MnO_2 nanoparticles, which may block the existing Li^+ host sites. Interestingly, the PSA of P-CNFs/PEDOT/MnO_2 was centered at 7.61 nm, which confirmed that the electrode was mainly composed of a mesoporous structure. The existence of numerous of mesopores can not only shorten the diffusion length for both Li^+ and electrons, but also act as a buffer medium to accommodate the volume change during cycling (Li et al., 2020a).

Raman spectroscopy studies of the P-CNFs, P-CNFs/MnO_2, P-CNFs/PEDOT and P-CNFs/PEDOT/MnO_2 composites were carried out and the results are displayed in Fig. 4b. Two primary peaks located at 1340 cm^{-1} and 1585 cm^{-1} were identified in all spectra, corresponding to D (the disordered structure of C material) and G bands (the graphitized C) (Tao et al., 2019). Intensity ratio of D and G bands (I_D/I_G) was employed to determine the degree of graphitization in carbonaceous material (Chen et al., 2017). $I_D/I_G$was calculated to be 0.96 (P-CNFs), 1.01 (P-CNFs/PEDOT), 0.92 (P-CNFs/MnO_2) and 0.99 (P-CNFs/PEDOT/MnO_2), respectively. A relatively high I_D/I_G value indicates low crystalline nature of C component in the composite, which provides an effective diffusion pathway for Li^+ with additional Li-storage sites (Samuel et al., 2017; Liu et al., 2014). These results are consistent with the XRD results which will be discussed later.

XRD patterns shown in Fig. 4c were measured to evaluate the crystallinity of the prepared samples. In P-CNFs spectrum, a broad peak emerged at $2\theta = 25°$, representing the (002) plane of graphite-like layers in the fibers (Yahya et al., 2019). The XRD pattern of PEDOT showed a diffraction peak at $2\theta = 24°$ (020), indicating its typical amorphous structure and π-π interaction of thiophene rings along the polymer backbone. However, the characteristic peak of PEDOT was not easy to be distinguished in the P-CNFs/PEDOT spectrum, due to the overlap with typical CNFs peak. Moreover, other peaks marked with ♦ symbol [2θ = 21.7° (110), 25.0° (220), 29.2° (310), 35.3° (130), 40.4°

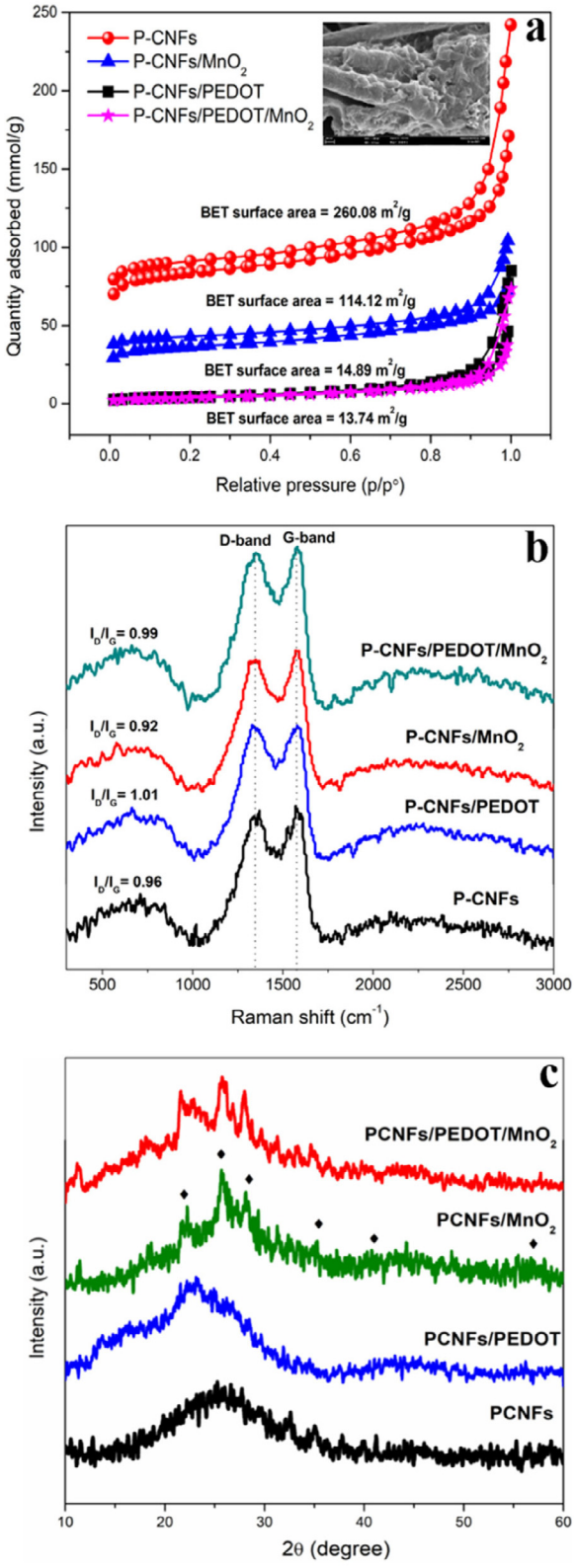

Fig. 4. (a) N_2 adsorption and desorption isotherm curves for (a) P-CNFs, P-CNFs/MnO_2, P-CNFs/PEDOT and P-CNFs/PEDOT/MnO_2 composites. Inset: high-magnification FESEM image of P-CNFs/PEDOT/MnO_2 composite. (b) Raman spectra of the as-obtained P-CNFs, P-CNFs/MnO_2, P-CNFs/PEDOT and P-CNFs/PEDOT/MnO_2 composites. (c) XRD patterns of P-CNFs, P-CNFs/MnO_2, P-CNFs/PEDOT and P-CNFs/PEDOT/MnO_2 electrodes.

(210), 57.1° (240)] in PCNFs/MnO_2 spectrum were indexed to the crystallographic planes of MnO_2 with tetragonal phase (JCPDS 44–0141). Notably, all diffraction peaks representing PCNFs, PEDOT and MnO_2 were clearly observed in the diffractogram of PCNFs/PEDOT/MnO_2.

Chemical compositions and the oxidation states of P-CNFs/PEDOT/MnO_2 were examined by XPS analysis, as shown in Fig. 5. The full-survey XPS spectrum in Fig. 5a indicates the coexistence of C, Mn, O and S elements, matching well with the elemental mapping analysis. In Fig. 5b, the C1*s* XPS spectrum can be deconvoluted into peaks located at 283.6, 284.4, 285.4 and 288.3 eV, which correspond to C=C, C–C, C–O–C and C=O (Xie et al., 2019), respectively. In addition, the high-resolution Mn2*p* spectrum (Fig. 5c) exhibits two characteristic peaks at 641.3 ($Mn2p_{3/2}$) and 653.5 eV ($Mn2p_{3/2}$), with a spin–orbit level energy spacing of 11.8 eV, which reveals the presence of Mn^{4+} valence state (Zhi et al., 2016). The O1*s* core level spectrum (Fig. 5d) displays three peaks with binding energy at 530.0 eV, 530.9 eV and 531.7 eV, corresponding to Mn—O—Mn, C—O—C (Liu et al., 2017) and C=O functional groups (Liu et al., 2019a), respectively. As for the S2*p* spectrum (Fig. 5e), two prominent peaks located at 163.5 and 168.7 eV were attributed to the positively charged S within the thiophene ring of PEDOT structure (Du et al., 2018).

3.2. Electrochemical performance of P-CNFs/PEDOT/MnO_2 electrodes and Li-ion cells

Before assembly CR2032 coin type half-cells (Fig. 6a) to study the performance of the newly developed electrodes, fundamental electrochemical studies were carried out. The CV curves of P-CNFs/PEDOT/MnO_2 electrode during the first five cycles are shown in Fig. 6b, with data collected in the potential range between 0.1 and 3.0 V *vs.* Li^+/Li, at a scan rate of 0.1 mV/s. In the first cathodic scanning process, three reduction peaks appeared at 0.3, 1.0 and 1.5 V (*vs.* Li^+/Li), corresponding to Li^+ intercalation in P-CNFs ($C_6 + Li^+ + e^- \rightarrow LiC_6$), accompanied with the reduction of Mn^{4+} into Mn^{2+}($MnO_2 + 2Li^+ + 2e^- \rightarrow MnO + Li_2O$), the creation of SEI film (Yang et al., 2020) and the intercalation of Li^+ within PEDOT structure. The formation of unstable SEI film could be a concrete reason for the large first cycle irreversible capacity upon charging–discharging (Liu et al., 2015; Di et al., 2021; Hao et al., 2020). In addition, the main reduction peak of PEDOT slightly shifted from 1.3 V to 1.5 V. This was probably related to the activation of electrode and interaction between outermost PEDOT nanoparticles and P-CNFs layer. On the inverse process, the de-lithiation processes of both LiC_6 (Yan et al., 2021) and Mn oxide are observed at the oxidation peak around 1.2 V (*vs.* Li^+/Li), while another oxidation peak at 2.2 V (*vs.* Li^+/Li) was related to de-lithiation process of PEDOT; these signals nearly overlapped in subsequent cycles. Except for the first cycle, it is observed the shapes of the CV curves were maintained in the following (2^{nd}- 5^{th}) cycles, suggesting an excellent electrochemical reversibility of P-CNFs/PEDOT/MnO_2 electrode with stable Li^+ insertion/extraction mechanisms (Ma et al., 2020; Yan et al., 2020). Fig. 6c depicts the voltage–capacity curves of the P-CNFs, P-CNFs/MnO_2, P-CNFs/PEDOT and P-CNFs/PEDOT/MnO_2 electrodes at a current density of 2.0 mA/g. As illustrated, P-CNFs/PEDOT/MnO_2 displays the highest discharge and charge specific capacities of 1477 mAh/g and 698 mAh/g, respectively, in the initial cycle, which was comparable with the theoretical value (≈1792 mAh/g). A significant improvement in Li storage performance of P-CNFs/PEDOT/MnO_2 electrode was mainly ascribed to the synergistic cooperation all of its individual constituents in which P-CNFs offered abundant of active sites for Li^+ insertion, PEDOT enhanced the electronic conductivity of the electrode material and MnO_2 could ideally possess a high theoretical capacity.

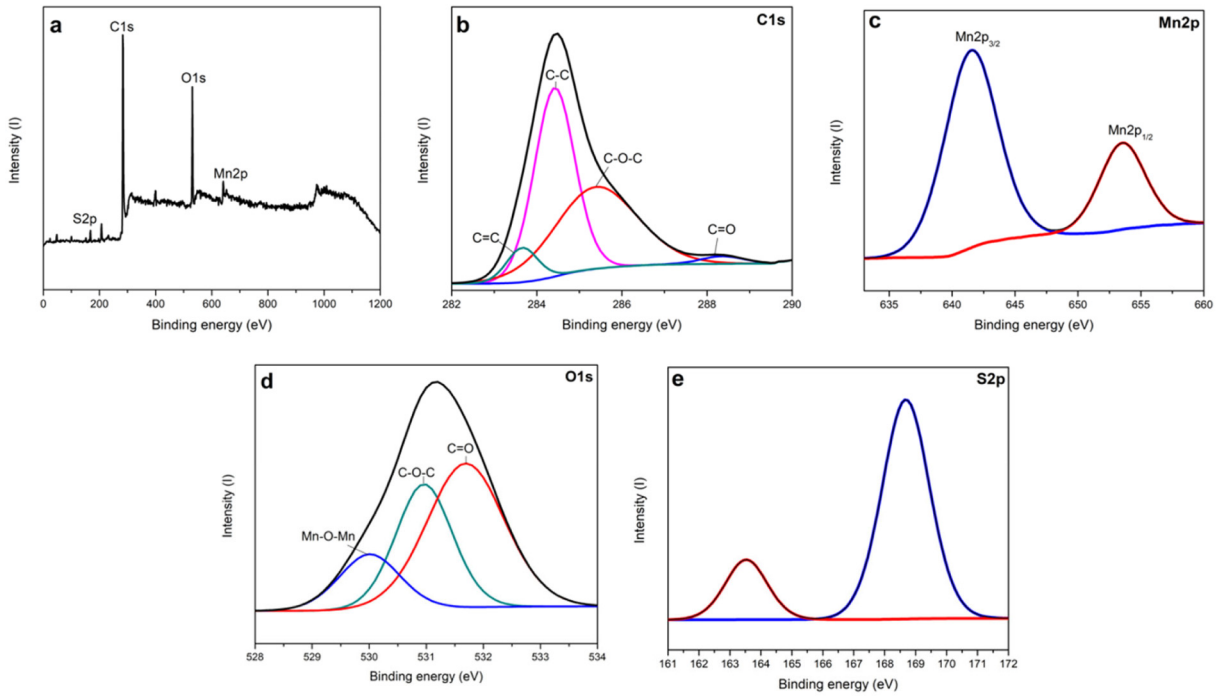

Fig. 5. (a) XPS wide-spectra curve; high-resolution XPS spectra of (b) C1*s*, (c) Mn2*p*, (d) O1*s* and (e) S2*p* of P-CNFs/PEDOT/MnO_2 composite.

Moreover, according to Zhang et al., the inclusion of conductive PEDOT coated on zinc ferrite ($ZnFe_2O_4$-PEDOT) via *in situ* polymerization displayed a greatly enhanced discharge capacity of 1087 mAh/g in comparison with pure $ZnFe_2O_4$ (710 mAh/g) at a current density of 1.0 A/g (Zhang et al., 2020). The result proved that PEDOT nanoparticles played a crucial role in increasing the conductivity as well as improving the transmission rate of electrons and ions. However, the initial irreversible capacity loss could be attributed to the generation of the SEI layer (Li et al., 2020b; Lu et al., 2020) and the formation of lithium oxide (Li_2O) since it continuously consumed Li during discharge process. Fig. 6d represents the cycling performance of all four samples at 0.2 mA/g for 20 cycles. Despite the highest initial discharge capacity, P-CNFs/PEDOT/MnO_2 electrode showed a severe capacity decay from 1477 mAh/g to 204 mAh/g (capacity retention of 13.8%, see **Figure S2**) after 20 repetitive cycling, which could be attributed to one of the following reasons. First, the formation of inevitable and fractured SEI film with partial decomposition of electrolyte can significantly restrict the Li^+ and electron transportation (Wang et al., 2015). Second, the tendency of PEDOT nanostructure to undergo rapid fracture and pulverization due to large volume variation (expansion/shrinkage) upon cycling reduces the intimate contact between the electrode constituents. Although preliminary work of half-cell P-CNFs/PEDOT/MnO_2 electrode underwent rapid capacity decay over the cycles, the discharge capacity of P-CNFs/PEDOT/MnO_2 was still above the theoretical capacity of graphite (≈372 mAh/g) until 8^{th} cycle of charge/discharge and stable in the following cycles. This provides an interesting insight to be a potential replacement or additives for the existing commercialized carbon-based LIBs anodes. Interestingly, the Coulombic efficiencies of all samples (Fig. 6e) exceeded 90% after the initial cycle and remained constant in the subsequent cycles, thus further clarifying their excellent electrochemical reversibility. It was noted that all samples exhibited low Coulombic efficiency only in the first cycle, which could be attributed to the formation of unstable SEI layer and electrode pulverization during charge/discharge cycling (Wan and Hu, 2019). To be noted, the formation process setting in this study is not separated during the charge/discharge analysis. In addition, the parallel work on charge/discharge at high current density (15 mA/g) for P-CNFs/PEDOT/MnO_2 electrode is represented in **Figure S3**. It is noteworthy that the first discharge capacity of half-cell P-CNFs/PEDOT/MnO_2 was 501 mAh/g. Although the capacity of P-CNFs/PEDOT/MnO_2 at the current density of 15 mA/g was lower than 2 mA/g, the sample showed an improved capacity retention of about 62.8%, while the Coulombic efficiency was maintained between 90 and 100% over 20 cycles. To further examine the electrochemical properties of the assembled electrodes, EIS analysis was carried out before cycling and after cycling, as displayed in Fig. 6f–g. As shown in Fig. 6f, all curves are composed of a semicircle at high frequency region, the intercept value of the horizontal axis and an inclined line at low frequency region which corresponded to charge transfer resistance (R_{ct}), electrolyte resistance (R_e) and Warburg diffusion (W) of Li^+ within the electrode, respectively. A simulated equivalent circuit model (inset of Fig. 6g) displayed two parallel resistance-capacitor (RC) circuits, R_e and W elements in series. In this model, R_2//CPE_2 (where CPE = constant phase element) represents R_{ct} resulting from the diffusion of ions at the electrolyte/electrode interface and non-ideal double layer capacitance. Meanwhile, for the second semicircle, R_1//CPE_1 refers to the contact resistance and CPE of SEI layer. The obtained R_{ct} values (Table 2) for P-CNFs, P-CNFs/MnO_2, P-CNFs/PEDOT and P-CNFs/PEDOT/MnO_2 before cycling were 24.16, 41.83, 24.40 and 24.50 Ω, respectively. Higher R_{ct} obtained from P-CNFs/MnO_2 electrode could be attributed to the poor electrical conductivity of MnO_2 and the formation of unstable SEI film on the electrode surface (Cheng et al., 2020). However, the inclusion of conductive PEDOT significantly enhanced the electron transport and intrinsic conductivity of P-CNFs/PEDOT/MnO_2, which facilitated Li^+ diffusion throughout the cycling process. The Nyquist plots of all electrode samples after 20 charge/discharge cycles are shown in Fig. 6g. From the Nyquist plots, it can be seen that P-CNFs/PEDOT electrode exhibited the highest R_{ct} value of 232.66 Ω, compared to P-CNFs/MnO_2(169.17 Ω), P-CNFs/PEDOT/MnO_2(131.91 Ω) and P-CNFs (52.14 Ω). This could be attributed to the structural destruction caused by the repetitive swelling and shrinkage behavior of PEDOT during cycling, hence leading to severe capacity

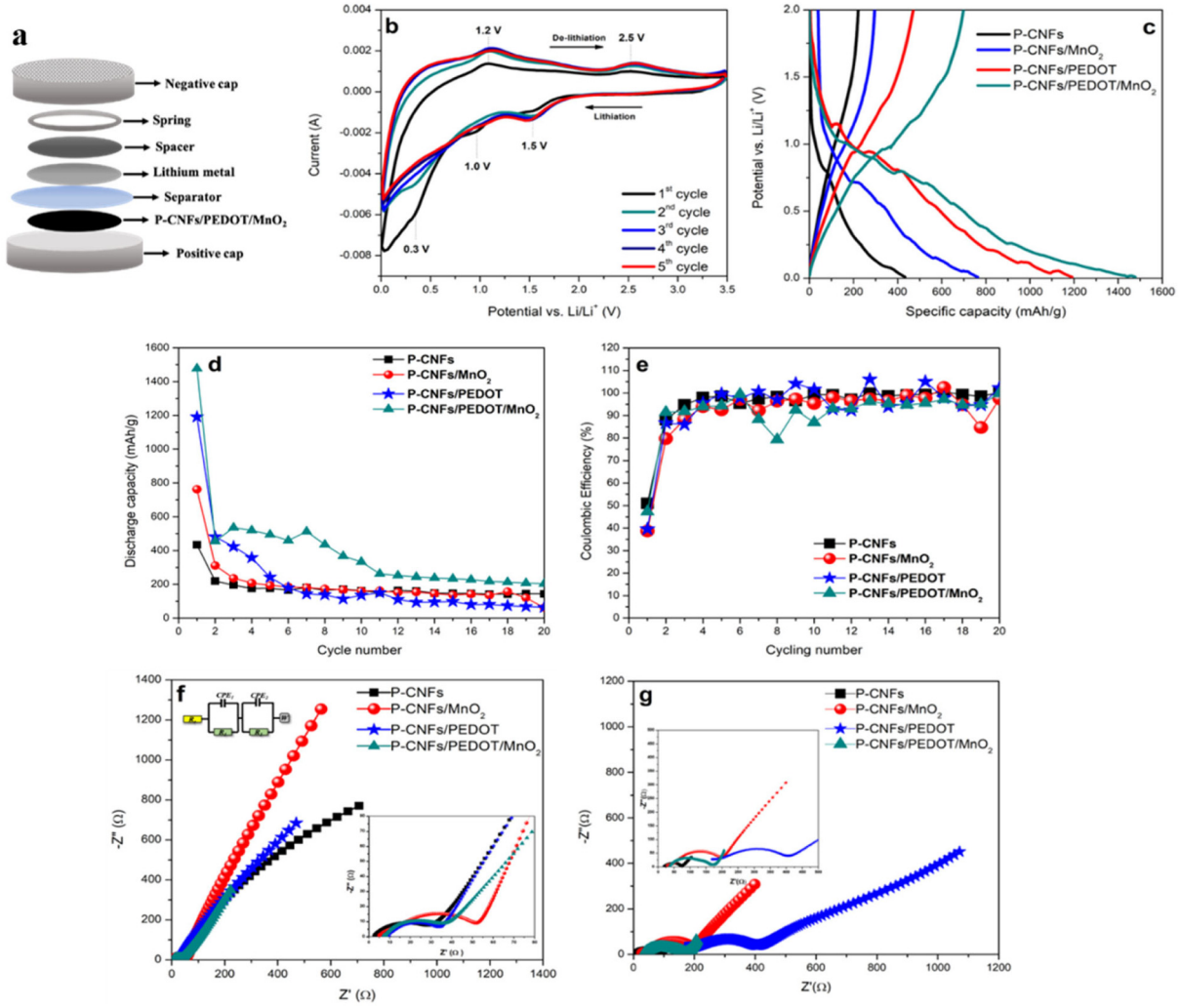

Fig. 6. (a) Schematic representation of CR2032 coin type half-cell assembly. (b) CV curves of the assembled P-CNFs/PEDOT/MnO_2/Li half-cell at a scanning rate of 0.1 mV/s. (c) First galvanostatic charge/discharge, (d) cycling performance and (e) Coulombic efficiency of all prepared electrodes at a current density of 2.0 mA/g. Nyquist plots of P-CNFs, P-CNFs/MnO_2, P-CNFs/PEDOT and P-CNFs/PEDOT/MnO_2 electrodes recorded from 1.0 MHz to 0.01 Hz (f) before and (g) after charge and discharge cycles. The inset of panel (f) indicates the equivalent circuit used for fitting the experimental data.

decay and inferior cyclability. In contrast with P-CNFs electrode, which shows a slight increase in R_e and R_{ct} values, it may be due to the unique 3D network of P-CNFs, which could not only enhance the electron conductivity, but also maintain the structural stability during repeated discharge and charge process.

In addition, as shown in Table 2, P-CNFs/PEDOT/MnO_2 electrode exhibited the lowest W and relaxation time (τ) after 20 cycles of charge/discharge. This proved that the inclusion of PEDOT in P-CNFs/MnO_2 system could reduce Li^+ diffusion length (Chong et al., 2019) and accelerate the migration of Li^+ through the SEI film on the surface of active material.

These results are really intriguing if the future integration with energy conversion devices and the exploitation in post-lithium batteries are considered (Lavagna et al., 2021; Rahman et al., 2021; Amici et al., 2021; Bella et al., 2021; Baiano et al., 2020; Massaro et al., 2020).

4. Conclusion

In summary, this research demonstrates a novel development of P-CNFs/PEDOT/MnO_2 anode for LIBs using an intriguing combination of electrospinning, carbonization and subsequent electrodeposition techniques. The surface morphology and physicochemical properties of as-prepared samples are examined by FESEM, Raman spectroscopy, AFM, BET, XRD and XPS analysis. The unique architecture of P-CNFs/PEDOT/MnO_2 electrode endows an outstanding capability for LIBs by displaying a discharge specific capacity of 1477 mAh/g, higher than P-CNFs/PEDOT (1191 mAh/g), P-CNFs/MnO_2 (763 mAh/g) and P-CNFs (433 mAh/g) at a current density 2.0 mA/g. Although the capacity of P-CNFs/PEDOT/MnO_2 electrode was gradually decreased in the continuous cycles, the Coulombic efficiency was enhanced above than 90% after the initial cycle, interestingly and reproducibly showing its electrochemical reversibility. Moreover, after 20 cycles of charge/discharge, P-CNFs/PEDOT/MnO_2 electrode showed a slightly increment of R_{ct} (from 24.50 to 131.91 Ω), a value lower than that of P-CNFs/PEDOT (232.66 Ω) and P-CNFs/MnO_2 (169.17 Ω). The favorable electrochemical performance of P-CNFs/PEDOT/MnO_2 can be ascribed to the synergistic effect between P-CNFs, PEDOT and MnO_2, which promoted more active sites for electrochemical reactions. This improved the electrical conductivity and prevented the volume variation upon charge/discharge process, respectively. Hence, with further improvement P-CNFs/PEDOT/MnO_2 and together with the advantages of simple, low-cost fabrication and promising performance of P-CNFs/PEDOT/MnO_2, this new material could be a potential

Table 2
The impedance parameters of P-CNFs, P-CNFs/MnO_2, P-CNFs/PEDOT and P-CNFs/PEDOT/MnO_2 electrodes before and after cycling.

Electrode	Before cycling				After cycling			
	R_s (Ω)	R_{ct} (Ω)	τ (s)	W (S $s^{1/2}$)	R_s (Ω)	R_{ct} (Ω)	τ (s)	W (S $s^{1/2}$)
P-CNFs	2.99	24.16	3.32×10^{-5}	0.0171	19.62	52.14	0.0012	0.0545
P-CNFs/MnO_2	5.09	41.83	0.0013	5.56×10^{6}	27.39	169.17	0.0013	1.52×10^{6}
P-CNFs/PEDOT	8.70	24.40	0.0012	7.52×10^{5}	167.51	232.66	0.0004	2.61×10^{6}
P-CNFs/PEDOT/MnO_2	7.06	24.50	0.0025	0.05154	35.52	131.91	3.32×10^{-5}	0.0491

replacement or additive for the existing high-performance anode materials for LIB application.

CRediT authorship contribution statement

Muhammad Amirul Aizat Mohd Abdah: Investigation, Writing – original draft, Writing – review & editing, Conceptualization. **Marliyana Mokhtar:** Investigation, Writing – review & editing. **Lee Tian Khoon:** Investigation, Writing – review & editing. **Kamaruzzaman Sopian:** Investigation, Writing – review & editing. **Nurul Akmaliah Dzulkurnain:** Investigation, Writing – review & editing. **Azizan Ahmad:** Writing – review & editing, Funding acquisition, Conceptualization, Resources. **Yusran Sulaiman:** Writing – review & editing, Resources. **Federico Bella:** Writing – review & editing, Funding acquisition, Conceptualization. **Mohd Sukor Su'ait:** Supervision, Writing – review & editing, Funding acquisition, Conceptualization.

Declaration of competing interest

The authors declare that they have no known competing financial interests or personal relationships that could have appeared to influence the work reported in this paper.

Data availability

The raw/processed data required to reproduce these findings cannot be shared at this time as the data also forms part of an ongoing study.

Acknowledgments

Authors would like to thank Universiti Kebangsaan Malaysia for permitting this research and financial support by a UKM Modal Insan grant (MI-2020-009) and Dana Lonjakan Penerbitan SERI. Special gratitude to SERI and CRIM UKM as well as Dr. Yusran's laboratory in UPM for research facilities. We would like to acknowledge the Research Center for Quantum Engineering Design, Faculty of Science and Technology, Universitas Airlangga, Surabaya (Indonesia) for appointing Prof. Azizan Ahmad as a visiting professor. Politecnico di Torino is gratefully acknowledged by F.B. for granting the fund named "Contributo ERC per chi ha superato il primo step di valutazione".

Appendix A. Supplementary data

Supplementary material related to this article can be found online at https://doi.org/10.1016/j.egyr.2021.10.110.

References

Amici, J., Torchio, C., Versaci, D., Dessantis, D., Marchisio, A., Caldera, F., Bella, F., Francia, C., Bodoardo, S., 2021. Nanosponge-based composite gel polymer electrolyte for safer Li-O_2batteries. Polymers 13, 1625.

Ao, L., Wu, C., Xu, Y., Wang, X., Jiang, K., Shang, L., Li, Y., Zhang, J., Hu, Z., Chu, J., 2020. A novel sn particles coated composite of SnO_x/ZnO and N-doped carbon nanofibers as high-capacity and cycle-stable anode for lithium-ion batteries. J. Alloys Compd. 819, 153036.

Augustine, C.A., Panoth, D., Paravannoor, A., 2019. High performance Li-ion battery anodes based on Si nano core in an LATP matrix with better electrolyte compatibility and temperature resistance. ChemistrySelect 4, 7090–7095.

Bai, Y., Tang, Y., Gao, Y., Li, X., Liu, L., Zhang, Y., Gao, S., 2019. Bamboo-like porous CNTs encapsulated $Zn_3V_3O_8$ nanoparticles as high-performance anodes for lithium ion batteries. J. Alloys Compd. 798, 678–684.

Baiano, C., Schiavo, E., Gerbaldi, C., Bella, F., Meligrana, G., Talarico, G., Maddalena, P., Pavone, M., Muñoz García, A.B., 2020. Role of surface defects in CO_2adsorption and activation on $CuFeO_2$ delafossite oxide. Mol. Catal. 496, 111181.

Baumann, M., Barelli, L., Passerini, S., 2020. The potential role of reactive metals for a clean energy transition. Adv. Energy Mater. 10, 2001002.

Bella, F., De Luca, S., Fagiolari, L., Versaci, D., Amici, J., Francia, C., Bodoardo, S., 2021. An overview on anodes for magnesium batteries: challenges towards a promising storage solution for renewables. Nanomaterials 11, 810.

Carley, S., Konisky, D.M., 2020. The justice and equity implications of the clean energy transition. Nat. Energy 5, 569–577.

Chen, R., Qu, W., Guo, X., Li, L., Wu, F., 2016. The pursuit of solid-state electrolytes for lithium batteries: from comprehensive insight to emerging horizons. Mater. Horiz. 3, 487–516.

Chen, J., Wu, X., Gong, Y., Wang, P., Li, W., Tan, Q., Chen, Y., 2017. Synthesis of Mn_3O_4/N-doped graphene hybrid and its improved electrochemical performance for lithium-ion batteries. Ceram. Int. 43, 4655–4662.

Chen, L., Zhang, M., Ding, Y., Wu, S., Li, Y., Liang, G., Li, H., Pan, H., 2021. Estimation the internal resistance of lithium-ion-battery using a multi-factor dynamic internal resistance model with an error compensation strategy. Energy Rep. 7, 3050–3059.

Cheng, Z., Hu, Y., Wu, K., Xing, Y., Pan, P., Jiang, L., Mao, J., Ni, C., Wang, Z., Zhang, M., Zhang, Y., Gu, X., Zhang, X., 2020. Si/TiO_2/Ti_2O_3 composite carbon nanofiber by one-step heat treatment with highly enhanced ion/electron diffusion rates for next-generation lithium-ion batteries. Electrochim. Acta 337, 135789.

Chong, B.M., Azman, N.H.N., Abdah, M.A.A.M., Sulaiman, Y., 2019. Supercapacitive performance of N-doped graphene/Mn_3O_4/Fe_3O_4 as an electrode material. Appl. Sci. 9, 1040.

Choudhury, S., Tu, Z., Nijamudheen, A., Zachman, M.J., Stalin, S., Deng, Y., Zhao, Q., Vu, D., Kourkoutis, L.F., Mendoza-Cortes, J.L., Archer, L.A., 2019. Stabilizing polymer electrolytes in high-voltage lithium batteries. Nat. Commun. 10, 3091.

Di, F., Wang, N., Li, L., Geng, X., Yang, H., Zhou, W., Sun, C., An, B., 2021. Coral-like porous composite material of silicon and carbon synthesized by using diatomite as self-template and precursor with a good performance as anode of lithium-ions battery. J. Alloys Compd. 854, 157253.

Du, F.P., Cao, N.N., Zhang, Y.F., Fu, P., Wu, Y.G., Lin, Z.D., Shi, R., Amini, A., Cheng, C., 2018. PEDOT:PSS/graphene quantum dots films with enhanced thermoelectric properties via strong interfacial interaction and phase separation. Sci. Rep. 8, 6441.

Fantham, T.L., Gladwin, D.T., 2021. An overview of safety for laboratory testing of lithium-ion batteries. Energy Rep. 7, 2–8.

Galluzzo, M.D., Maslyn, J.A., Shah, D.B., Balsara, N.P., 2019. Ohm's law for ion conduction in lithium and beyond-lithium battery electrolytes. J. Chem. Phys. 151, 020901.

Gao, J., Lowe, M.A., Abruña, H.D., 2011. Spongelike nanosized Mn_3O_4 as a high-capacity anode material for rechargeable lithium batteries. Chem. Mater. 23, 3223–3227.

H. Huang, X., Tu, J.P., Xia, X.H., Wang, X.L., Xiang, J.Y., Zhang, L., 2010. Porous NiO/poly(3,4-ethylenedioxythiophene) films as anode materials for lithium ion batteries. J. Power Sources 195, 1207–1210.

Hannan, M.A., Lipu, M.S.H., Hussain, A., Mohamed, A., 2017. A review of lithium-ion battery state of charge estimation and management system in electric vehicle applications: challenges and recommendations. Renew. Sustain. Energy Rev. 78, 834–854.

Hao, R., Wang, J., Yao, S., Lan, Y., Li, D., Feng, X., 2020. The 3D networked $MnCO_3$-C composite as anode materials for lithium ion batteries. J. Electroanal. Chem. 877, 114655.

Hao, Z., Zhao, Q., Tang, J., Zhang, Q., Liu, J., Jin, Y., Wang, H., 2021. Functional separators towards the suppression of lithium dendrites for rechargeable high-energy batteries. Mater. Horiz. 8, 12–32.

Hu, J., Xu, Z., Li, X., Liang, S., Chen, Y., Lyu, L., Yao, H., Lu, Z., Zhou, L., 2020. Partially graphitic hierarchical porous carbon nanofiber for high performance supercapacitors and lithium ion batteries. J. Power Sources 462, 228098.

Hui, Y., Cao, L., Xu, Z., Huang, J., Ouyang, H., Li, J., Hu, H., 2017. In situ synthesis of core-shell $Li_4Ti_5O_{12}$ @ polyaniline composites with enhanced rate performance for lithium-ion battery anodes. J. Mater. Sci. Technol. 33, 231–238.

Jin, Y., He, W., Ren, F., Ren, P., Xu, Y., 2019. High-performance symmetric lithium-ion batteries constructed with a new bi-functional electrode Li- and Mn-rich layered oxide $0.3Li_2MnO_3{\cdot}0.7LiNi_{1/3}Co_{1/3}Mn_{1/3}O_2$. Electrochim. Acta 325, 134932.

Jin, R., Liu, J., Qiu, H., Xu, C., Weng, L., Liu, C., Zeng, Y., 2020. Synthesis of porous nanosheet-assembled $ZnFe_2O_4$@polypyrrole yolk-shell microspheres as anode materials for high-rate lithium-ion batteries. J. Electroanal. Chem. 863, 114038.

Ju, J., Zhao, H., Kang, W., Tian, N., Deng, N., Cheng, B., 2017. Designing MnO_2 & carbon composite porous nanofiber structure for supercapacitor applications. Electrochim. Acta 258, 116–123.

Jung, H.R., Lee, W.J., 2011. Ag/poly(3,4-ethylenedioxythiophene) nanocomposites as anode materials for lithium ion battery. Solid State Ion. 187, 50–57.

Khoon, L.T., Fui, M.L.W., Hassan, N.H., Su'ait, M.S., Vedarajan, R., Matsumi, N., Bin Kassim, M., Shyuan, L.K., Ahmad, A., 2019. In situ sol–gel preparation of ZrO_2 in nano-composite polymer electrolyte of PVDF-HFP/MG49 for lithium-ion polymer battery. J. Sol-Gel Sci. Technol. 90, 665–675.

Kumar, R., Sahoo, S., Joanni, E., Singh, R.K., Yadav, R.M., Verma, R.K., Singh, D.P., Tan, W.K., Pérez del Pino, A., Moshkalev, S.A., Matsuda, A., 2019. A review on synthesis of graphene, h-BN and $MoS_2$for energy storage applications: recent progress and perspectives. Nano Res. 12, 2655–2694.

Lavagna, L., Syrrokostas, G., Fagiolari, L., Amici, J., Francia, C., Bodoardo, S., Leftheriotis, G., Bella, F., 2021. Platinum-free photoelectrochromic devices working with copper-based electrolytes for ultrastable smart windows. J. Mater. Chem. A 9, 19687–19691.

Lee, H.J., Lee, J., Park, S.M., 2010. Electrochemistry of conductive polymers. 45. Nanoscale conductivity of PEDOT and PEDOT:PSS composite films studied by current-sensing AFM. J. Phys. Chem. B 114, 2660–2666.

Lee, T.K., Zaini, N.F.M., Mobarak, N.N., Hassan, N.H., Noor, S.A.M., Mamat, S., Loh, K.S., KuBulat, K.H., Su'ait, M.S., Ahmad, A., 2019. PEO based polymer electrolyte comprised of epoxidized natural rubber material (ENR50) for Li-Ion polymer battery application. Electrochim. Acta 316, 283–291.

Lehmann, M.L., Yang, G., Gilmer, D., Han, K.S., Self, E.C., Ruther, R.E., Ge, S., Li, B., Murugesan, V., Sokolov, A.P., Delnick, F.M., Nanda, J., Saito, T., 2019. Tailored crosslinking of poly(ethylene oxide) enables mechanical robustness and improved sodium-ion conductivity. Energy Storage Mater. 21, 85–96.

Li, T., Bai, X., Gulzar, U., Bai, Y.J., Capiglia, C., Deng, W., Zhou, X., Liu, Z., Feng, Z., Proietti Zaccaria, R., 2019. A comprehensive understanding of lithium–sulfur battery technology. Adv. Funct. Mater. 29, 1901730.

Li, Z., Hu, X., Shi, Z., Lu, J., Wang, Z., 2020a. MOFs-derived metal oxides inlayed in carbon nanofibers as anode materials for high-performance lithium-ion batteries. Appl. Surf. Sci. 531, 147290.

Li, L., Liu, W., Dong, H., Gui, Q., Hu, Z., Li, Y., Liu, J., 2021. Surface and interface engineering of nanoarrays toward advanced electrodes and electrochemical energy storage devices. Adv. Mater. 33, 2004959.

Li, B., Wu, C., Hu, D., Xu, J., Zhang, T., Tong, J., Fang, X., 2020b. Copper extraction from the ammonia leach liquor of spent lithium ion batteries for regenerating $LiNi_{0.5}Co_{0.5}O_2$ by co-precipitation. Hydrometallurgy 193, 105310.

Liang, Y., Chen, L., Cai, L., Liu, H., Fu, R., Zhang, M., Wu, D., 2016. Strong contribution of pore morphology to the high-rate electrochemical performance of lithium-ion batteries. Chem. Commun. 52, 803–806.

Liao, H., Chen, H., Zhou, F., Zhang, Z., Chen, H., 2019. Dendrite-free lithium deposition induced by mechanical strong sponge-supported unique 3D cross-linking polymer electrolyte for lithium metal batteries. J. Power Sources 435, 226748.

Lin, J., Yu, L., Sun, Q., Wang, F., Cheng, Y., Wang, S., Zhang, X., 2020. Multiporous core-shell structured MnO@N-doped carbon towards high-performance lithium-ion batteries. Int. J. Hydrogen Energy 45, 1837–1845.

Liu, A., Guan, Y., Guo, Z., Che, H., Wang, L., Li, H., Feng, Z., Zhang, Z., Zhang, X., Wang, G., Mu, J., 2019a. Carbon/MoO_2@MoS_2 ternary synergetic systems: heterojunction structures with effective self-built electric fields for high-performance lithium ion batteries. Solid State Ionics 340, 115021.

Liu, B., Hu, X., Xu, H., Luo, W., Sun, Y., Huang, Y., 2014. Encapsulation of MnO nanocrystals in electrospun carbon nanofibers as high-performance anode materials for lithium-ion batteries. Sci. Rep. 4, 4229.

Liu, J., Kopold, P., vanAken, P.A., Maier, J., Yu, Y., 2015. Energy storage materials from nature through nanotechnology: a sustainable route from reed plants to a silicon anode for lithium-ion batteries. Angew. Chem. Int. Ed. 54, 9632–9636.

Liu, X., Li, H., Li, D., Ishida, M., Zhou, H., 2013. PEDOT Modified $LiNi_{1/3}Co_{1/3}Mn_{1/3}O_2$ with enhanced electrochemical performance for lithium ion batteries. J. Power Sources 243, 374–380.

Liu, L., Qi, X., Yin, S., Zhang, Q., Liu, X., Suo, L., Li, H., Chen, L., Hu, Y.S., 2019b. In situ formation of a stable interface in solid-state batteries. ACS Energy Lett. 4, 1650–1657.

Liu, D., Rahman, M.M., Ge, C., Kim, J., Lee, J.J., 2017. Highly stable and conductive PEDOT:PSS/graphene nanocomposites for biosensor applications in aqueous medium. New J. Chem. 41, 1558–15465.

Lu, W., Cong, L., Liu, Y., Liu, J., Mauger, A., Julien, C.M., Sun, L., Xie, H., 2020. Pseudocapacitance controlled fast-charging and long-life lithium ion battery achieved via a 3D mutually embedded VPO_4/rGO electrode. J. Alloys Compd. 812, 152135.

Ma, Y., Liu, P., Xie, Q., Zhang, C., Wang, L., Peng, D.L., 2020. Intrinsic performance regulation in hierarchically porous Co_3O_4 microrods towards high-rate lithium ion battery anode. Mater. Today Energy 16, 100383.

Massaro, A., Muñoz García, A.B., Maddalena, P., Bella, F., Meligrana, G., Gerbaldi, C., Pavone, M., 2020. First-principles study of Na insertion at TiO_2anatase surfaces: new hints for Na-ion battery design. Nanoscale Adv. 2, 2745–2751.

Mohd Abdah, M.A.A., Azman, N.H.N., Kulandaivalu, S., Abdul Rahman, N., Abdullah, A.H., Sulaiman, Y., 2019. Potentiostatic deposition of poly(3, 4-ethylenedioxythiophene) and manganese oxide on porous functionalised carbon fibers as an advanced electrode for asymmetric supercapacitor. J. Power Sources 444, 227324.

Ogawa, H., Mori, H., 2019. In-situ formation of poly(ionic liquid)s with ionic liquid-based plasticizer and lithium salt in electrodes for solid-state lithium batteries. Polymer 178, 121614.

Ouyang, H., Ma, Y., Gong, Q., Li, C., Huang, J., Xu, Z., Wei, B., 2020. Tailoring porous structure and graphitic degree of seaweed-derived carbons for high-rate performance lithium-ion batteries. J. Alloys Compd. 823, 153862.

Rahman, N.A., Hanifah, S.A., Mobarak, N.N., Ahmad, A., Ludin, N.A., Bella, F., Su'ait, M.S., 2021. Chitosan as a paradigm for biopolymer electrolytes in solid-state dye-sensitised solar cells. Polymer 230, 124092.

Rowden, B., Garcia-Araez, N., 2021. Estimating lithium-ion battery behavior from half-cell data. Energy Rep. 7, 97–103.

Samuel, E., Jo, H.S., Joshi, B., An, S., Park, H.G., Il Kim, Y., Yoon, W.Y., Yoon, S.S., 2017. Decoration of MnO nanocrystals on flexible freestanding carbon nanofibers for lithium ion battery anodes. Electrochim. Acta 231, 582–589.

Shadike, Z., Tan, S., Wang, Q.C., Lin, R., Hu, E., Qu, D., Yang, X.Q., 2021. Review on organosulfur materials for rechargeable lithium batteries. Mater. Horiz. 8, 471–500.

Song, H.J., Kim, J.C., Choi, M., Choi, C., Dar, M.A., Lee, C.W., Park, S., Kim, D.W., 2015. Li_2MnSiO_4 nanorods-embedded carbon nanofibers for lithium-ion battery electrodes. Electrochim. Acta 180, 756–762.

Sun, C., Ruan, Y., Zha, W., Li, W., Cai, M., Wen, Z., 2020. Recent advances in anodic interface engineering for solid-state lithium-metal batteries. Mater. Horiz. 7, 1667–1696.

Tao, L., Huang, Y., Zheng, Y., Yang, X., Liu, C., Di, M., Larpkiattaworn, S., Nimlos, M.R., Zheng, Z., 2019. Porous carbon nanofiber derived from a waste biomass as anode material in lithium-ion batteries. J. Taiwan Inst. Chem. Eng. 95, 217–226.

Tran, C., Kalra, V., 2013. Fabrication of porous carbon nanofibers with adjustable pore sizes as electrodes for supercapacitors. J. Power Sources 235, 289–296.

Wan, H., Hu, X., 2019. Nitrogen/sulfur co-doped disordered porous biocarbon as high performance anode materials of lithium/sodium ion batteries. Int. J. Hydrogen Energy 44, 22250–22262.

Wang, S., Fernandez, C., Yu, C., Fan, Y., Cao, W., Stroe, D.I., 2020. A novel charged state prediction method of the lithium ion battery packs based on the composite equivalent modeling and improved splice Kalman filtering algorithm. J. Power Sources 471, 228450.

Wang, J.G., Yang, Y., Huang, Z.H., Kang, F., 2015. MnO-carbon hybrid nanofiber composites as superior anode materials for lithium-ion batteries. Electrochim. Acta 170, 164–170.

Xie, J., Xia, J., Yuan, Y., Liu, L., Zhang, Y., Nie, S., Yan, H., Wang, X., 2019. Sb_2S_3 embedded in carbon–silicon oxide nanofibers as high-performance anode materials for lithium-ion and sodium-ion batteries. J. Power Sources 435, 226762.

Xu, C., Puente-Santiago, A.R., Rodríguez-Padrón, D., Muñoz Batista, M.J., Ahsan, M.A., Noveron, J.C., Luque, R., 2021. Nature-inspired hierarchical materials for sensing and energy storage applications. Chem. Soc. Rev. 50, 4856–4871.

Xu, B., Saianand, G., Roy, V.A.L., Qiao, Q., Reza, K.M., Kang, S.W., 2019. Employing PCBTDPP as an efficient donor polymer for high performance ternary polymer solar cells. Polymers 11, 1423.

Xu, D., Wang, P., Yang, R., 2017. Enhanced electrochemical performance of core-shell $Li_4Ti_5O_{12}$/PTh as advanced anode for rechargeable lithium-ion batteries. Ceram. Int. 43, 7600–7606.

Yahya, N., Kamarudin, S.K., Karim, N.A., Masdar, M.S., Loh, K.S., Lim, K.L., 2019. Durability and performance of direct glycerol fuel cell with palladium-aurum/vapor grown carbon nanofiber support. Energy Convers. Manage. 188, 120–130.

Yan, Z., Jiang, L., Chen, D., Huo, B., Zhou, H., Huang, Z., 2021. Nitrogen doped carbon nanotubes supported Co_9S_8 nanoparticles for lithium-ion batteries with excellent electrochemical performance. Mater. Lett. 282, 128850.

Yan, J., Xu, P., Chen, S., Wang, G., Zhang, F., Zhao, W., Zhang, Z., Deng, Z., Xu, M., Yun, J., Zhang, Y., 2020. Construction of highly ordered ZnO microrod@SnO_2 nanowire heterojunction hybrid with a test-tube brush-like structure for high performance lithium-ion batteries: experimental and theoretical study. Electrochim. Acta 330, 135312.

Yan, H., Zhang, G., Li, Y., 2017. Synthesis and characterization of advanced $Li_3V_2(PO_4)_3$ nanocrystals@conducting polymer PEDOT for high energy lithium-ion batteries. Appl. Surf. Sci. 393, 30–36.

Yang, Y., Yang, H.X., Wu, Y.Q., Pu, H., Meng, W.J., Gao, R.Z., Zhao, D.L., 2020. Graphene caging core-shell Si@Cu nanoparticles anchored on graphene sheets for lithium-ion battery anode with enhanced reversible capacity and cyclic performance. Electrochim. Acta 341, 136037.

Yao, M., Liu, A., Xing, C., Li, B., Pan, S., Zhang, J., Su, P., Zhang, H., 2020. Asymmetric supercapacitor comprising a core-shell $TiNb_2O_7$@MoS_2/C anode and a high voltage ionogel electrolyte. Chem. Eng. J. 394, 124883.

Zainoodin, A.M., Kamarudin, S.K., Masdar, M.S., Daud, W.R.W., Mohamad, A.B., Sahari, J., 2014. High power direct methanol fuel cell with a porous carbon nanofiber anode layer. Appl. Energy 113, 946–954.

Zhang, Y., Konya, M., Kutsuma, A., Lim, S., Mandai, T., Munakata, H., Kanamura, K., 2019a. Magnesium storage performance and mechanism of 2D-ultrathin nanosheet-assembled spinel $MgIn_2S_4$cathode for high-temperature Mg batteries. Small 15, 1902236.

Zhang, M., Liu, Y., Zhu, H., Wang, X., 2020. Hierarchical bead chain $ZnFe_2O_4$-PEDOT composites with enhanced Li-ion storage properties as anode materials for lithium-ion batteries. Appl. Surf. Sci. 529, 147078.

Zhang, J., Zhang, X., Hou, Z., Zhang, L., Li, C., 2019b. Uniform SiO_x/graphene composite materials for lithium ion battery anodes. J. Alloys Compd. 809, 151798.

Zhao, X., Mai, Y., Luo, H., Tang, D., Lee, B., Huang, C., Zhang, L., 2014. Nano-MoS_2/poly(3,4-ethylenedioxythiophene):poly(styrenesulfonate) composite prepared by a facial dip-coating process for Li-ion battery anode. Appl. Surf. Sci. 288, 736–741.

Zheng, L., Liu, Y., Lan, J., Yu, Y., Yang, X., 2017. Hierarchical heterostructure of interconnected ultrafine MnO_2 nanosheets grown on carbon-coated MnO nanorods toward high-performance lithium-ion batteries. Chem. Eng. J. 330, 1289–1296.

Zhi, J., Reiser, O., Huang, F., 2016. Hierarchical MnO_2 spheres decorated by carbon-coated cobalt nanobeads: low-cost and high-performance electrode materials for supercapacitors. ACS Appl. Mater. Interfaces 8, 8452–8459.

Zhou, G., Wu, C., Wei, Y., Li, C., Lian, Q., Cui, C., Wei, W., Chen, L., 2016. Tufted $NiCo_2O_4$ nanoneedles grown on carbon nanofibers with advanced electrochemical property for lithium ion batteries. Electrochim. Acta 222, 1878–1886.

Zhu, J., Ding, X., 2019. A facile one–pot synthesis of Sn/graphite/graphene nanocomposites as anode materials for lithium–ion batteries. J. Alloys Compd. 809, 151870.